INTERNATIONAL JOURNAL FOR NUMERICAL METHODS IN FLUIDS
Int. J. Numer. Meth. Fluids 2003; **42**:999–1026 (DOI: 10.1002/fld.570)

Direct testing of subgrid scale models in large-eddy simulation of a non-isothermal turbulent jet

C. Ferreira Gago[1,*,†], F. Garnier[2] and F. Utheza[3]

[1] *Ecole Nationale des Ponts et Chaussées, ENPC, Laboratoire CEREVE, 6 et 8, avenue Blaise Pascal, Cité Descartes, Champs-sur-Marne, Marne-la-Vallée 77455, France*
[2] *Office National d'Etudes et de Recherches Aérospatiales, ONERA, 29, avenue de la Division Leclerc, Châtillon 92320, France*
[3] *Laboratoire d'Etudes des Transferts d'Energie et de Matière-LETEM, Université de Marne-la-Vallée, Bâtiment Lavoisier, rue Galilée, 77454 Marne-la-Vallée Cédex 02, France*

SUMMARY

A comparative assessment of subgrid models of compressible large-eddy simulations is performed for a temporally evolving heated round jet at a low Mach number. Initially, the temperature difference with respect to the ambient is chosen according to the one at the nozzle exit of a typical aircraft engine. Subgrid modelling in both the momentum and the energy equations is then necessary to close the problem. As basic models, we have considered the compressible versions of the Smagorinsky model, the mixed-scale model (which can be defined as a dynamic-type model) and the similarity model. The first two models are also supplemented with the similarity model or/and a selective function. Large-eddy simulations (LES) results are compared with those obtained from a direct numerical simulation (DNS). Thus to allow correspondence between DNS and LES the Reynolds number, in the present study, is still not very high and equal to 500. Among the cases investigated the hybrid Smagorinsky model (linear combination of the Smagorinsky model and the similarity model) displays the best performances, especially when dealing with the turbulent stresses and the turbulent heat flux. Copyright © 2003 John Wiley & Sons, Ltd.

KEY WORDS: large-eddy simulation; direct numerical simulation; temporal simulation; turbulent jet; subgrid scale models; heated jet; low subsonic

1. INTRODUCTION

The study of heated round jets is relevant for many aerospace applications, such as the jet propulsion efficiency, the jet exhaust noise reduction and the atmospheric impact of aircraft exhaust pollutants [1–3]. Since the jet behaviour is dominated by the action of turbulence, the properties of the flow are difficult to measure or foresee analytically. Therefore, it is desirable to develop methods, which must be able to predict with acceptable confidence the

*Correspondence to: C. Ferreira Gago, Ecole Nationale des Ponts et Chaussées, Laboratoire CEREVE, 6 et 8, avenue Blaise Pascal, Cité Descartes-Champs-sur-Marne, Marne-la-Vallée 77455, France.
† E-mail: ferreira@cereve.enpc.fr

Received 26 May 2002
Revised 19 February 2003

evolution of the jet flow. Recently, with the advance of computing power, it has become possible to conduct Direct Numerical Simulations (DNS) of jets. However, DNS of jet flows are limited to low Reynolds numbers, well below the values of engineering interest. On the other hand, and as far as high Reynolds numbers are of concern, an intermediate approach could be used which is called Large-Eddy Simulation (LES). The contribution of the large scales of the turbulent flow is then computed exactly while the smallest scales or subgrid scales (SGS) of turbulence are modelled, according to the well-known Kolmogorov assumption of their universal behaviour. Although the idea of scale separation between the large and the small ones appears somewhat schematic, the LES technique is essentially based on solving the turbulent scales which are large enough to contain the energy-carrying information about the flow configuration (i.e. flow geometry and boundary conditions). So, LES appears as a promising numerical technique to simulate turbulent flows and it is seen as a method midway between exact simulations (DNS) and time average modelled computations (RANS).

The two major difficulties in LES approach are mostly the insufficient grid resolution and the inadequate SGS models. Indeed, most of the SGS models are deduced from incompressible isotropic theory, and give satisfactory results when applied to such category of flows. However, if the dynamics of the flow differ much from this of isotropic turbulence, the SGS models must be examined in order to get the one which provides the most accurate prediction of the flow comportment.

A lot of DNS and LES of jet flows are available in literature [2, 4, 5], but very few are focused on the direct testing of subgrid scale models. One may quote for example the recent work of Le Ribault *et al.* [5], which presents *a posteriori* tests in the case of a spatially developing jet. The authors compare different subgrid models: the Smagorinsky model, the dynamic Smagorinsky model and the dynamic hybrid Smagorinsky model and conclude that dynamic hybrid Smagorinsky model provides the best results when comparing with the two others. However, in these studies, attention has been mostly given to the cases of isothermal jets while, within areas mentioned above, turbulent jets of interest are often non-isothermal. The effect of jet heating could be fundamental, as it was already proved for acoustic emissions. As a result, an experimental and theoretical investigation carried out by Tanna *et al.* [6] on heated supersonic, shock-free jets suggests that an additional source of noise could be attributed to density or temperature fluctuations.

So, the motivation of this work is precisely to compare the performances of different LES techniques, in the transitional regime of a low subsonic heated round jet. Following the dimensional analysis of Jacquin and Garnier [7], the initial mean temperature at the center of the jet is chosen according to the one at the nozzle exit of a typical aircraft engine. Subgrid modelling in both the momentum and the energy equations is then necessary to close the problem. The adequacy of nine subgrid models will be achieved by comparisons of LES results with those of DNS. In order to allow correspondence between DNS and LES, the Reynolds number in the present study is still not very high, but in the near future, we will conduct simulations at higher Reynolds number.

The numerical simulations of the flow are based on the use of three-dimensional temporal DNS and LES of the compressible Navier–Stokes equations. As a large extend in the stream-wise direction is required, indeed, we decide to investigate the case of a temporal jet. In a temporal simulation, the flow is computed in a reference frame moving at the mean flow speed and flow periodicity is assumed. The temporal jet evolution qualitatively exhibits the same physical phenomena as in the spatial case but requires an order of magnitude less

computational effort. Furthermore, some authors (see, for example, Reference [8]) have shown that the numerical simulation based on the time-dependent approach could be a useful tool for interpreting turbulence phenomena if some restrictions have been applied.

The structure of the paper is as follows. In Section 2, we start with the description of the governing equations used in DNS and LES, while Section 3 is devoted to the subgrid modelling. Next, in Sections 4 and 5, we focus on the numerical solutions techniques, including the initial and boundary conditions. The results of the calculations are discussed in Section 6, and the final section contains the conclusions from this work.

2. BASIC EQUATIONS

The systems of equations solved in the direct numerical simulations and in the large-eddy simulations are presented below.

The flow is governed by the fully compressible Navier–Stokes equations. The mass, momentum and total energy equations are written below in a familiar dimensionless form:

$$\partial_t \rho + \partial_j(\rho u_j) = 0 \tag{1}$$

$$\partial_t(\rho u_i) + \partial_j(\rho u_i u_j) + \partial_i p - \partial_j \sigma_{ij} = 0 \tag{2}$$

$$\partial_t E + \partial_j\{(E + p)u_j\} - \partial_j(\sigma_{ij} u_i) + \partial_j q_j = 0 \tag{3}$$

Symbols ∂_t and ∂_j denote the time derivative and divergence operator, respectively. The summation convention for repeated indices is used. t represents time and x_j spatial co-ordinates. Concerning the flow variables, the velocity vector is denoted by $\mathbf{u}$, while the density ρ, the pressure p and the temperature T are linked by the state law for perfect gas:

$$p = \rho T / \gamma M^2 \tag{4}$$

The viscous stress tensor is given by

$$\sigma_{ij} = \frac{\mu(T)}{Re} S_{ij} \tag{5}$$

S_{ij} is the strain rate:

$$S_{ij} = \partial_j u_i + \partial_i u_j - 2/3 \delta_{ij} \partial_k u_k \tag{6}$$

where δ_{ij} is the Kronecker delta, defined as

$$\delta_{ij} = 1 \text{ if } i = j \quad \text{and} \quad \delta_{ij} = 0 \text{ if } i \neq j \tag{7}$$

The fluid is assumed to be an ideal gas with a power law temperature-dependent viscosity [9]:

$$\mu(T) = T^{0.75} \tag{8}$$

E is the total energy density:

$$E = \frac{p}{\gamma - 1} + \frac{1}{2} \rho u_i u_i \tag{9}$$

q_j represents the heat flux:

$$q_j = \frac{-\mu(T)}{(\gamma - 1)Re\,Pr\,M^2}\frac{\partial T}{\partial x_j} \tag{10}$$

Re and M are the Reynolds and Mach numbers, respectively. The Prandtl number Pr and the ratio of specific heats $\gamma = Cp/Cv$ are set equal to 0.7 and 1.4, respectively, the admitted values for air.

We have assembled and tested a computer simulation code that can perform compressible large-eddy simulations or direct numerical simulations of Equations (1)–(3). In DNS these equations are solved directly on a fine grid. On the other hand, in the LES approach, these equations are filtered in order to reduce the number of scales to be solved, and the grid considered is coarser than in DNS. The LES part of the code is based on Vreman's decomposition [10], relevant elements of which we now review.

As recalled in Section 1, in LES the large, energy-carrying scales are computed directly, while the small, unresolved scales that tend to be isotropic (and hence more universal in nature) and their interaction with the large scales are modelled. In order to separate the large from the small scales, a filtering operation is used. The filter extracts the large scales from the entire flow field, so that a filtered (or resolved, or large scale) variable is denoted by an overbar and defined as follows:

$$\bar{f} = \int_\Omega G(\mathbf{x} - \xi; \Delta) f(\xi)\,\mathrm{d}\xi \tag{11}$$

where $\mathbf{x}$ and ξ are vectors in the entire domain Ω. The filter function G depends on the cut-off length scale Δ, and so determines the size of the small scales. G is assumed to commute with time and spatial derivatives and satisfies the condition:

$$\int_\Omega G(\mathbf{x} - \xi; \Delta)\,\mathrm{d}\xi = 1 \tag{12}$$

For compressible flows, it is usual to introduce the Favre average [11] defined as

$$\tilde{f} = \frac{\overline{\rho f}}{\bar{\rho}} \tag{13}$$

When applying the former operation to the governing equations (1)–(3), one obtains the filtered equations of motion, which are solved in LES. They take the following form:

$$\partial_t \bar{\rho} + \partial_j(\bar{\rho}\tilde{u}_j) = 0 \tag{14}$$

$$\partial_t(\bar{\rho}\tilde{u}_i) + \partial_j(\bar{\rho}\tilde{u}_i\tilde{u}_j) + \partial_i \bar{p} - \partial_j \hat{\sigma}_{ij} = -\partial_j A_1 + \partial_j A_2 \tag{15}$$

$$\partial_t \hat{E} + \partial_j\{(\hat{E} + \bar{p})\tilde{u}_j\} - \partial_j(\hat{\sigma}_{ij}\tilde{u}_i) + \partial_j \hat{q}_j = -B_1 - B_2 - B_3 + B_4 + B_5 + B_6 - B_7 \tag{16}$$

In this description, the left-hand sides of Equations (14)–(16) are the Navier–Stokes equations now expressed in terms of filtered variables. The right-hand sides contain the so-called subgrid terms. These subgrid terms represent the effects of unresolved scales of motion on the large

scales and need to be modelled. They are defined as:

$$A_1 = \tau_{ij} = \bar{\rho}(\widetilde{u_i u_j} - \tilde{u}_i \tilde{u}_j) \tag{17}$$

$$A_2 = \overline{\sigma_{ij}} - \hat{\sigma}_{ij} = \frac{\overline{\mu(T) S_{ij}}}{Re} - \frac{\mu(\tilde{T}) S_{ij}}{Re} \tag{18}$$

$$B_1 = \frac{1}{\gamma - 1} \partial_j (\overline{p u_j} - \bar{p} \tilde{u}_j) \tag{19}$$

$$B_2 = \overline{p \partial_k u_k} - \bar{p} \partial_k \tilde{u}_k \tag{20}$$

$$B_3 = \partial_j (\tau_{kj} \tilde{u}_k) \tag{21}$$

$$B_4 = \tau_{kj} \partial_j \tilde{u}_k \tag{22}$$

$$B_5 = \overline{\sigma_{kj} \partial_j u_k} - \overline{\sigma_{kj}} \partial_j \tilde{u}_k \tag{23}$$

$$B_6 = \partial_j (\overline{\sigma_{ij}} \tilde{u}_i - \hat{\sigma}_{ij} \tilde{u}_i) \tag{24}$$

$$B_7 = \partial_j (\overline{q_j} - \hat{q}_j) \tag{25}$$

The definitions of the filtered modified viscous stress tensor, strain rate, total energy density and heat flux are based on their non-filtered counter-part, so that:

$$\hat{\sigma}_{ij} = \frac{\mu(\tilde{T})}{Re} \tilde{S}_{ij} \tag{26}$$

$$\tilde{S}_{ij} = \partial_j \tilde{u}_i + \partial_i \tilde{u}_j - 2/3 \delta_{ij} \partial_k \tilde{u}_k \tag{27}$$

$$\hat{E} = \frac{\bar{p}}{\gamma - 1} + \frac{1}{2} \bar{\rho} \tilde{u}_i \tilde{u}_i \tag{28}$$

$$\hat{q}_j = \frac{-\mu(\tilde{T})}{(\gamma - 1) Re\, Pr\, M^2} \partial_j \tilde{T} \tag{29}$$

Finally, the system is closed with the filtered state law:

$$\bar{p} = \bar{\rho} \tilde{T} / \gamma M^2 \tag{30}$$

3. SUBGRID MODELLING

This section is devoted to the description of the subgrid models considered in the LES method. We will successively investigate the models used in the momentum and in the energy equations. In order to provide a point of reference for the subgrid models, we have also performed a DNS on the coarse LES grid. This calculation corresponds to the case in which the subgrid terms are simply omitted.

3.1. Momentum equation

As we will see through this paper, several assumptions allow us to simplify the LES governing equations by neglecting some subgrid terms. Firstly and as usually assumed in LES, the contribution of the subgrid term A_2, which results from the non-linearity of the viscous term, will not be accounted for [10]. Concerning the subgrid term A_1, namely the subgrid-scale tensor, nine models will be investigated.

3.1.1. The Smagorinsky model. The first model is the well-known Smagorinsky model [12] given by

$$\tau_{ij} = -\bar{\rho}\upsilon_{\mathrm{sm}} S_{ij}(\tilde{u}) \quad \text{with } \upsilon_{\mathrm{sm}} = (C_{\mathrm{s}}\Delta)^2 |S(\tilde{u})| \text{ and } |S(\tilde{u})|^2 = \tfrac{1}{2} S_{ij}(\tilde{u}) S_{ij}(\tilde{u}) \tag{31}$$

where S_{ij} is the strain rate defined by Equation (27). With respect to the Smagorinsky constant C_{s}, several values have been proposed. In our study, we take the value $C_{\mathrm{s}} = 0.2$, suggested by Clark *et al.* [13] and Deardoff [14] for the case of isotropic turbulence. The characteristic length scale is commonly chosen to be

$$\Delta = (\Delta_x \Delta_y \Delta_z)^{1/3} \tag{32}$$

where Δ_x, Δ_y and Δ_z are mesh sizes in the x, y and z directions, respectively.

This eddy viscosity model formally models the anisotropic part of the tensor τ_{ij} only, which is defined as

$$\tau_{ij}^{\mathrm{a}} = \tau_{ij} - \tfrac{1}{3} \tau_{kk} \delta_{ij} \tag{33}$$

Indeed, the Smagorinsky model was first developed for the LES of incompressible flows. In that previous case, the isotropic part of the tensor is usually not modelled but incorporated in the filtered pressure [10]. Thus the LES solves the modified pressure, while the (filtered) pressure itself remains unknown. For compressible flows, the pressure appears both in the momentum equation, the energy equation and in the equation of state, which makes the approach involving a modified pressure not feasible anymore. Consequently, in our study, we will simply neglect the isotropic part of the subgrid-scale tensor. Furthermore, according to Erlerbacher *et al.* [15] conclusions, the isotropic part of the subgrid-scale tensor is dominated by the thermodynamic pressure, so that it can be neglected without introducing appreciable errors. This hypothesis is assumed to remain valid for all the cases examined in our study. However, the Smagorinsky model, though very popular, has some notable drawbacks including the fact that it depends exclusively on large scales. This former feature turns this model too dissipative, specially when dealing with transitional flows [16].

3.1.2. The mixed-scale model. The excessive dissipation of the Smagorinsky model can be overcome if the model constant is replaced by a coefficient depending on both large and small scales of turbulence. Such model has been proposed by Sagaut *et al.* [17]. In this way, the mixed-scale model could be considered as a dynamic adjustment of the Smagorinsky coefficient. As the Smagorinsky model, the mixed-scale model is based on scalar subgrid viscosity now given by

$$\upsilon_{\mathrm{sm}} = C_{\mathrm{m}} |S|^{\alpha} (q_c^2)^{(1-\alpha)/2} \Delta^{(1+\alpha)} \tag{34}$$

where q_c^2 is the kinetic energy of the small scales evaluated by the following formula:

$$q_c^2 = \tfrac{1}{2}\,\tilde{u}_i'\tilde{u}_i' \tag{35}$$

The fluctuating resolved scales $\tilde{u}'$ are extracted from the resolved velocity field employing a discrete filter denoted by a wide hat:

$$\tilde{u}_i' = \tilde{u}_i - \hat{\tilde{u}}_i \tag{36}$$

The discrete filter is given by

$$\hat{\tilde{u}}_i = \tfrac{1}{4}\,\tilde{u}_{i-1} + \tfrac{1}{2}\,\tilde{u}_i + \tfrac{1}{4}\,\tilde{u}_{i+1} \tag{37}$$

It can be interpreted as a second-order approximation of a Gaussian filter whose characteristic length is $\hat{\Delta} = \sqrt{6}\Delta$ [18].

All the simulations presented in this article were performed with $\alpha = 0.5$ and $C_{\mathrm{m}} = 0.06$. These values are deduced from the Eddy Damped Quasi-Normal Markovian Theory in the isotropic case [19].

3.1.3. The similarity model. While eddy viscosity models may be able to represent the global dissipative effects of the small scales in a satisfactory way, they usually display very little correlation with the real subgrid scale stresses [19]. The similarity model, formulated by Bardina *et al.* [20] and revised by Liu *et al.* [21] is not of the eddy viscosity type and try to reproduce the details of the stresses more accurately. The premise of this model is that the significant interactions between the resolved scales of motion and the subgrid scales involve the smallest of the resolved scales and the largest of the subgrid scales. So that the structure of a tensor built from subgrid scales remains similar to these of the corresponding tensor evaluated from the smallest resolved scales. More specifically, the definition of subgrid scale tensor in terms of the unfiltered variables is applied to the filtered variables, so that the compressible extension of this model takes the form

$$\tau_{ij} = ((\bar{\rho}\tilde{u}_i\tilde{u}_j)\hat{} - (\bar{\rho}\tilde{u}_i)\hat{}\,(\bar{\rho}\tilde{u}_j)\hat{}/\hat{\bar{\rho}}) \tag{38}$$

The wide hat denotes the test filter given by Equation (37). This model underestimates the energy cascade from the filtered field to subgrid scales and does not lead to stable calculations [22]. However, in contrast to eddy viscosity models, the similarity model has a mechanism to represent backscatter of energy, from subgrid to resolved scales [23].

3.1.4. Hybrid models. The linear combination of an eddy viscosity-type model and the similarity model provides an hybrid model, written below in its compressible version:

$$\tau_{ij} = 0.5(-\bar{\rho}\upsilon_{\mathrm{sm}}S_{ij}(\tilde{u}) + ((\bar{\rho}\tilde{u}_i\tilde{u}_j)\hat{} - (\bar{\rho}\tilde{u}_i)\hat{}\,(\bar{\rho}\tilde{u}_j)\hat{}/\hat{\bar{\rho}})) \tag{39}$$

The subgrid scale viscosity is provided either by the Smagorinsky model or the mixed-scale model to constitute the hybrid Smagorinsky model or the hybrid mixed-scale model, respectively. Hybrid models take advantage of both the similar and eddy viscosity-type models. They correlate well with the real subgrid scale stresses and dissipates adequately the energy in the small scales [19].

3.1.5. Selective function. As previously recalled, subgrid modelling is mainly based on the isotropic nature of the unresolved scales. David [24] introduces a structural sensor (selective function) which is able to identify the regions of the flow where the former assumption is effectively verified. This selective function only applied to models involving a subgrid viscosity. The idea is to switch off the eddy viscosity when the flow is not three-dimensional enough. Let us denote θ the angle between the local filtered vorticity ($\tilde{\omega} = \nabla \times \tilde{u}$) and the local averaged filtered vorticity ($\hat{\tilde{\omega}} = \nabla \times \hat{\tilde{u}}$, the wide hat denotes the test filter given by Equation (37)). The three-dimensionalization criterion is based on the variations of this angle. More precisely and according to David, if the value of θ exceeds $\theta_0 = 20°$, the eddy viscosity is turned on. Otherwise, only molecular dissipation acts. In our study, we will consider the selective function proposed by Sagaut and Troff [25] and defined as

$$f_{\theta_0} = \begin{cases} 1 & \text{if } \theta \geqslant \theta_0 \\ r(\theta)^n & \text{else} \end{cases} \tag{40}$$

The calculations presented hereafter have been performed using $n = 2$ [19] and r is written as follows:

$$r(\theta) = \frac{\tan^2(\theta/2)}{\tan^2(\theta_0/2)} \tag{41}$$

Furthermore, pointing out the fact that the angle θ can be expressed as a function of the local filtered vorticity $\tilde{\omega}$, the local averaged filtered vorticity $\hat{\tilde{\omega}}$ and the local fluctuating filtered vorticity $\tilde{\omega}'$ can be defined as

$$\tilde{\omega}' = \tilde{\omega} - \hat{\tilde{\omega}} \tag{42}$$

$$\tilde{\omega}'^2 = (\hat{\tilde{\omega}})^2 + \tilde{\omega}^2 - 2 \times \tilde{\omega} \times (\hat{\tilde{\omega}}) \times \cos\theta \tag{43}$$

and taking into account the trigonometric relation:

$$\tan^2(\theta/2) = \frac{1 - \cos\theta}{1 + \cos\theta} \tag{44}$$

which becomes:

$$\tan^2(\theta/2) = \frac{2 \times \tilde{\omega} \times \hat{\tilde{\omega}} - (\hat{\tilde{\omega}})^2 - \tilde{\omega}^2 + (\tilde{\omega}')^2}{2 \times \tilde{\omega} \times \hat{\tilde{\omega}} + (\hat{\tilde{\omega}})^2 + \tilde{\omega}^2 - (\tilde{\omega}')^2} \tag{45}$$

The selective function acts as a multiplying factor for the subgrid viscosity, that leads to a new modified subgrid viscosity given by

$$\upsilon_{\text{sms}} = \upsilon_{\text{sm}} \times f_{\theta_0} \tag{46}$$

Finally, the names of the models with their abbreviations are listed in Table I.

3.2. Energy equation

The filtered equations for compressible flow have subgrid terms both in the momentum and energy equation. In the previous paragraph we focussed on the modelling of the dominant

Table I. Subgrid models for the turbulent stress tensor.

Model	Abbreviation
No model	NM
Smagorinsky	SM
Mixed Scale	MSM
Similarity	BM
Hybrid Smagorinsky	HSM
Hybrid Mixed Scale	HMSM
Selective Smagorinsky	SSM
Selective Mixed Scale	SMSM
Selective Hybrid Smagorinsky	SHSM
Selective Hybrid Mixed Scale	SHMSM

subgrid term in the momentum equation, the turbulent stress tensor. The subgrid terms in the filtered energy equation are the subject of this paragraph. First of all, following the *a priori* tests performed by Vreman [10], the subgrid terms B_6 and B_7, created by the non-linearities in the viscous stress and heat flux, respectively, can be neglected. The subgrid term B_2 is purely a compressibility effect since it vanishes if the flow is divergence free with constant density. Sarkar *et al.* [26] have shown, through direct numerical simulations of isotropic compressible turbulence, that the influence of B_2 is negligible. Finally, subgrid models for B_1, B_3, B_4 and B_5 are necessary to close the problem.

The subgrid term B_1 involves the filtered pressure and the filtered velocity. It represents the effect of subgrid scales on the conduction of heat in the large scales. In the case of an eddy viscosity-type model, it is modelled as follows:

$$B_1 = -\frac{\partial}{\partial x_j}\left\{\frac{\bar{\rho}\upsilon_{sm}}{(\gamma-1)Pr_t M^2}\frac{\partial \tilde{T}}{\partial x_j}\right\} \tag{47}$$

The value of the turbulent Prandtl number is set equal to 0.7 [27].

If a similarity model is used (the wide hat denotes the test filter given by Equation (37)) then

$$B_1 = \frac{1}{(\gamma-1)\gamma M^2}\frac{\partial}{\partial x_j}\{(\bar{\rho}\tilde{T}\tilde{u}_j)\hat{} - (\bar{\rho}\tilde{T})\hat{}(\bar{\rho}\tilde{u}_j)\hat{}/\hat{\bar{\rho}}\} \tag{48}$$

We can also adopt an hybrid model defined as

$$B_1 = \frac{1}{2}\frac{\partial}{\partial x_j}\left\{-\frac{\bar{\rho}\upsilon_{sm}}{(\gamma-1)Pr_t M^2}\frac{\partial \tilde{T}}{\partial x_j} + \frac{1}{(\gamma-1)\gamma M^2}\{(\bar{\rho}\tilde{T}\tilde{u}_j)\hat{} - (\bar{\rho}\tilde{T})\hat{}(\bar{\rho}\tilde{u}_j)\hat{}/\hat{\bar{\rho}}\}\right\} \tag{49}$$

If an hybrid model is used for B_1 the subscript 'T' will be added to the name of the model.

The SGS terms B_3 and B_4 depend directly upon the subgrid-scale tensor, they are thus obtained in a straightforward manner reporting the expression used to model the former tensor in Equations (21) and (22).

The subgrid term B_5 also intervenes in the transport equation for the subgrid scale kinetic energy k, investigated by Ghosal *et al.* [28]. Following this reference we model the term by

$$B_5 = C_\varepsilon \bar{\rho} \frac{k^{3/2}}{\Delta} \tag{50}$$

With

$$k = \frac{\tau_{ll}}{2\bar{\rho}} \tag{51}$$

C_ε is a dynamic coefficient which is assumed to be a function of time only. The procedure used to determine the former coefficient is that of Vreman [10]. It is based on the global balance of the terms in the integrated k-equation, which leads to

$$C_\varepsilon = \frac{\int_\Omega ((1-\gamma)B_1 + B_3 - B_4)\,\mathrm{d}\Omega}{\int_\Omega \bar{\rho}\,\dfrac{k^{3/2}}{\Delta}\,\mathrm{d}\Omega} \tag{52}$$

For models involving an eddy viscosity k is evaluated as [28]:

$$k = \frac{v_{\mathrm{sm}}^2}{\Delta^2} \tag{53}$$

For the similarity model, k is rather equal to q_c given by Equation (35).

4. NUMERICAL METHODS AND BOUNDARY CONDITIONS

The present section details the numerical solution techniques used to solve the compressible Navier–Stokes equations. The algorithm remains the same whatever the method considered, i.e. direct numerical simulation or large-eddy simulation.

Calculations are performed by using a sixth-order compact scheme in space for convective terms [29]. In order to minimize the aliasing error, we follow the procedure applied by Boersma and Lele [30]. Thus, the non-linear terms have been rewritten in the skew symmetric form i.e.:

$$\frac{\partial \rho u_i u_j}{\partial x_j} = \frac{1}{2}\left(\frac{\partial \rho u_i u_j}{\partial x_j} + u_i \frac{\partial \rho u_j}{\partial x_j} + \rho u_j \frac{\partial u_i}{\partial x_j}\right) \tag{53'}$$

Diffusive terms are discretized by using a second-order accurate finite difference scheme. This also helps to damp plausible instabilities. The time integration is carried out with a third-order Runge–Kutta method [31].

The formulation of suitable conditions to take into account all the information passing inward and outward across the boundaries, while minimizing spurious reflections, constitutes one of the principal difficulties in the simulation of unsteady flows in a truncated open computational domain. The non-reflexive conditions introduced by Thompson [34] attempts to meet these requirements and are used at the lateral boundaries of the computational domain. In the axial (i.e. streamwise) direction, periodicity is assumed, as usually done in temporal developing jet flows. The wavelength in the streamwise direction, i.e. the length of our control volume, is based on Michalke and Hermann's [32] inviscid linearized stability analysis

for spatially evolving jet. The large-scale structure of turbulence in a circular jet is dominated by the axisymmetric and first-order azimuthal components of turbulence. In order to observe the development of an instability, the length of the computational domain must be an even multiple of the instability's wavelength. Michalke and Hermann give the wavelength of maximum growth of the first azimuthal disturbance. Furthermore, Gaster [33] establishes a relation between the frequency and amplification rates for a disturbance growing with respect to time and those of a spatially growing wave having the same wave-number. So by using Gaster's transformation, we obtain the wavelength of maximum growth of the first azimuthal disturbance for a temporally evolving jet. Finally, in order to observe two pairing events, the downstream size of the computational domain is taken equal to fourth this wavelength.

5. COMPUTATIONAL PARAMETERS

The subject of the present study is a Mach 0.2 round jet exiting into an infinite domain. The equations presented in Section 2 are non-dimensionalized by scaling the velocities with the centreline velocity and the length scale is equal to the radius R. The former is expressed as the middle of the jet shear layer defined by

$$U(R) = \tfrac{1}{2}(U_j + U_0) \tag{54}$$

where U_j and U_0 are the jet core velocity and the external flow velocity, respectively. In the following, we use the initial velocity profile:

$$U(r) = \frac{1}{2}(U_j + U_0) - \frac{1}{2}(U_j - U_0)\tanh\left\{\frac{1}{4}\frac{R}{\theta}\left(\frac{r}{R} - \frac{R}{r}\right)\right\} \tag{55}$$

The distance r is related to the Cartesian co-ordinates by the relation:

$$r = \sqrt{x^2 + z^2} \tag{56}$$

θ denotes the momentum boundary layer thickness of the jet shear layer:

$$\theta = \int_0^\infty \left\{\frac{U - U_0}{U_j - U_0}\right\}\left\{1 - \frac{U - U_0}{U_j - U_0}\right\} \mathrm{d}r \tag{57}$$

Note that the static case $U_0 = 0$ has been investigated by several authors [35–37] and seems to model the circular jet flow in the potential core region quite well as shown by Moore [38]. We restrict the present investigation to one value of the jet parameter, namely $R/\theta = 10$. Indeed, among the cases studied by Michalke and Hermann [32], this value corresponds to the most unstable jet velocity profile. Random Gaussian shape perturbations are imposed on the three components of the velocity field. Other reference values are the centreline values for the density ρ_j, the temperature T_j, and the viscosity μ_j. Based on this, the Reynolds number is $Re_j = \rho_j U_j R/\mu_j = 500$. It is sufficiently high to allow transition to turbulence, and reasonably low to enable an accurate DNS to be performed. The initial mean temperature is provided by the Crocco–Busemann relation [9], and the jet temperature ratio is $T_j/T_0 = 2$ [7], where the subscript $()_0$ indicates a constant ambient quantity. The initial mean pressure is constant.

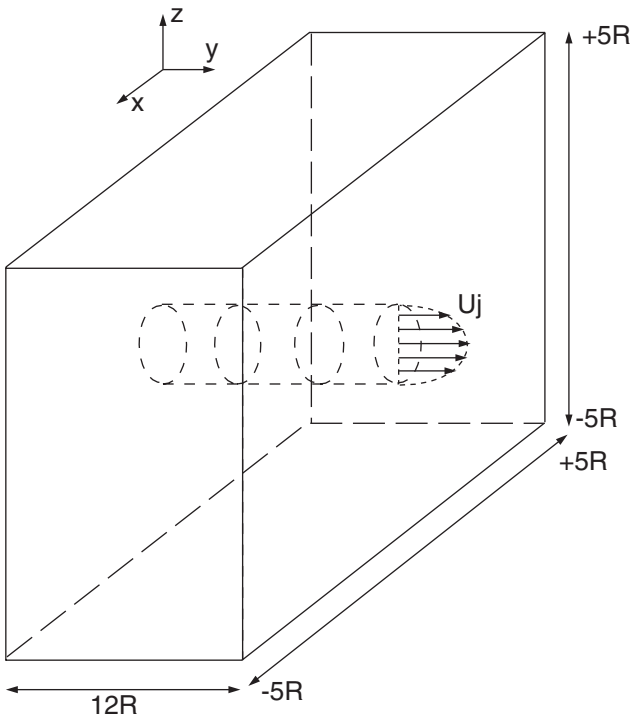

Figure 1. Schematic of the flow configuration.

The computational domain is rectangular and the grid is uniform in all directions. The cross plane extends from $x,z=-5R$ to $5R$ and, as explained in the previous section, the streamwise extent of the computational box is $L_y=12R$. A schematic of the flow configuration is presented in Figure 1. The DNS is conducted on a fine grid $(201\times201\times201)$ corresponding to a mesh of $\Delta_y=0.06R$ and $\Delta_{x,z}=0.05R$. On the other hand, LES calculations are performed on a coarser grid $(81\times81\times81)$ corresponding to $\Delta_y=0.15R$ and $\Delta_{x,z}=0.125R$. The Courant–Friedrichs–Lewy number is 0.6. The time step is $\Delta_t=0.005$ and 0.0125 for DNS and LES, respectively.

For computing the mean flow profiles, the simulated data, which is in Cartesian co-ordinates (x,y,z), is transformed to cylindrical co-ordinates (r,θ,y) using a higher-order cubic spline interpolation formula.

6. RESULTS AND DISCUSSION

Results are presented for the turbulent jet flow calculations and subgrid model performances are evaluated by comparisons with our direct numerical simulation. In the first part, the accuracy of the DNS as well as the transition of the jet flow to a fully turbulent state are briefly discussed. The second part is devoted to LES validations. The issues discussed deal with the different processes involved in the growth of instabilities. Both the mean and

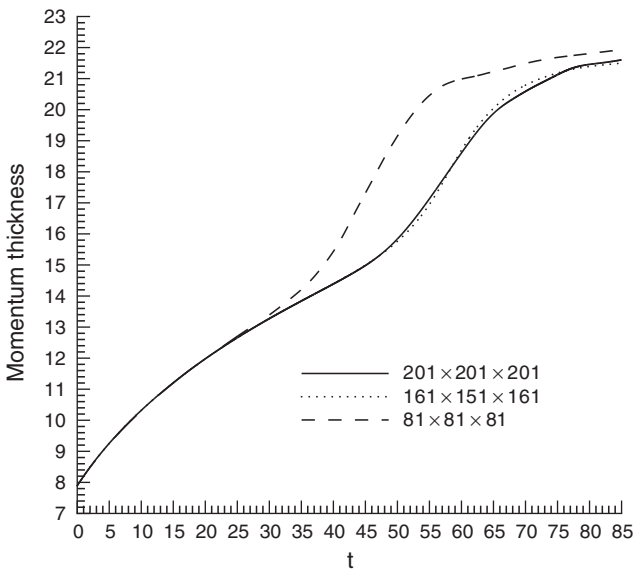

Figure 2. Temporal evolution of the momentum thickness for direct numerical simulations performed on a fine ($201 \times 201 \times 201$), a medium ($161 \times 151 \times 161$) and a coarse grid ($81 \times 81 \times 81$).

the turbulent quantities are examined. These include dynamics variables, such as the mean axial velocity or the turbulent stresses, but also quantities directly related to temperature: the temporal evolution of centreline temperature and turbulent heat flux.

Relevant scales for the validation of an LES simulation are the resolved ones. Thus, the comparison between LES and DNS results must involve these scales only. In other words, DNS simulation should be filtered. Many authors proceed in this way (see, for example, References [5] or [39]). Here, we have chosen to directly confront the LES results with the DNS ones. Indeed, the effective filter associated with LES remaining unknown, the choice of a filter to be applied to the DNS becomes somewhat ambiguous. However, we have experimented the effect of a Gaussian filter upon our DNS simulation. Differences between filtered and non-filtered DNS have not lead to convincing conclusions. Moreover, filtered DNS results have not provided a better agreement with the LES ones (data not shown).

6.1. DNS calculation

In order to investigate the influence of resolution, three grids were considered, a fine ($201 \times 201 \times 201$) a medium ($161 \times 151 \times 161$) and a coarse one ($81 \times 81 \times 81$). The temporal evolution of the momentum thickness is displayed in Figure 2, for the three meshes described above. The resolution of the finer grid is found sufficient. Indeed, the results obtained with the finer and the medium grids are almost identical (within less than 1% of relative error). On the other hand, the large differences (the maximum relative error is about 20%) observed between the results of the finer and the coarser grid, show that the resolution of the coarser grid is clearly inadequate.

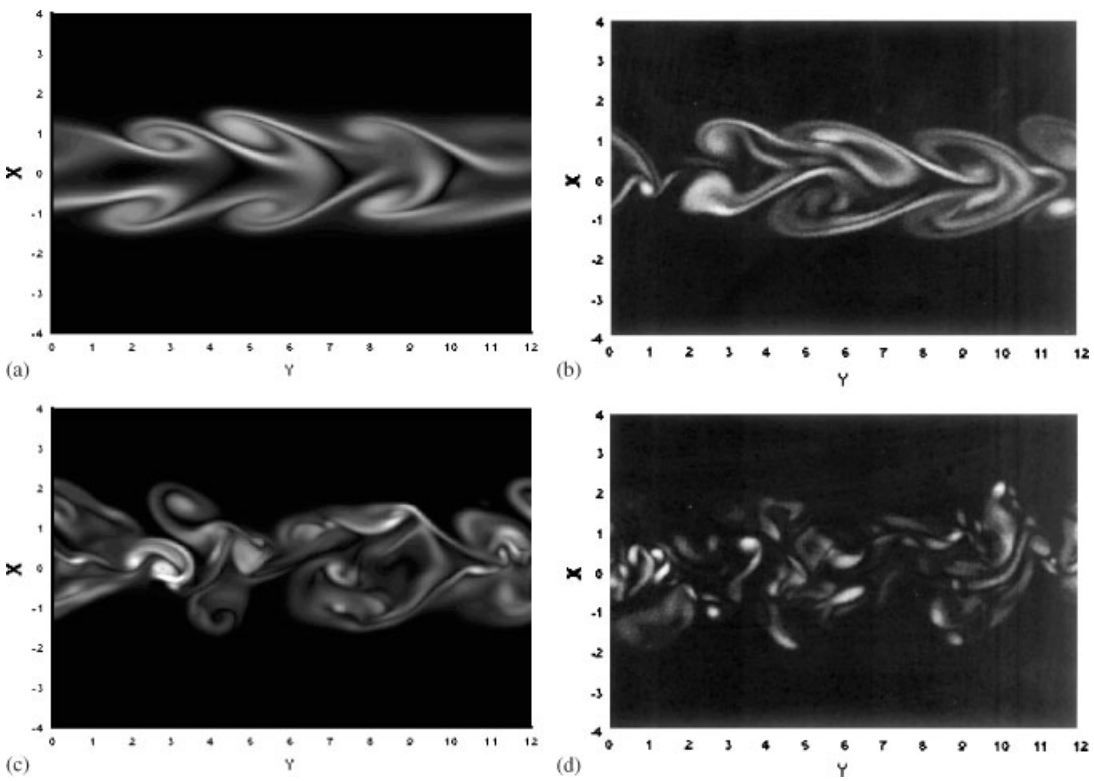

Figure 3. Vorticity magnitude contour plots in a meridional plane parallel to the axial direction: (a) $t = 55$, (b) $t = 65$, (c) $t = 75$, (d) $t = 85$. Contour range from 0.1 to 3 in steps of 0.1.

Transition processes occurring in the jet flow can be highlighted by the visualization of the vorticity magnitude contour plots, presented in Figure 3. The latter clearly illustrates the growth of instabilities and transition to fully developed turbulence. Initially, the vorticity is confined into a circular sheet. As perturbations grow, vorticity rolls up and accumulates in large vortex rings (Figure 3(a)). Later pairs of neighbouring rings merge (Figure 3(b)). Indeed, this process is particularly evident for the rings located at $y = 2$ and 5 in Figure 3(a) which merge, as observed in Figure 3(b). The breakdown of these large structures occurs before a second pairing event can take place (Figure 3(c)). Then the flow is mainly composed by small scales and exhibits a complicated disordered behaviour (Figure 3(d)). Other authors have already investigated these mechanisms. One may quote the work of Verzicco and Orlandi [40] and more recently that of Vreman *et al.* [39]. Figure 3 also demonstrates that all relevant scales are accurately represented on the fine grid.

6.2. LES validation

As already explained, LES computations will be done on the coarser grid and the adequacy of a subgrid model will be achieved by a comparison of the LES results with those of the DNS computed on the finer grid referred to as the well resolved DNS in the following. The

large differences, previously observed in Figure 2 between DNS calculations performed on the finer and on the coarser grid, illustrate that there is something to improve upon. Then the subgrid model will be considered to be bad if its contribution does not ameliorate the results obtained with the DNS on coarser grid (NM), and considered to be good if, on the contrary, it does.

6.2.1. Evolution of mean velocity and temperature fields. A comparison of the subgrid models with respect to the temporal evolution of the mean centreline velocity and mean centreline temperature is given in Figures 4 and 5. These mean values are computed in this paper as follows. First, the instantaneous field is averaged in the homogeneous direction y. Second, the averaged value is interpolated into a polar grid. Third, the later value is averaged in the azimuthal θ direction, to obtain a mean profile, which is function of r. No averaging in time is performed, therefore the mean profile is function of time. The values depicted in Figures 4 and 5 correspond to the mean profiles at the location $r = 0$. The typical evolutions of the mean centreline velocity and temperature are retrieved. In the potential core region, centreline velocity and temperature keep their maximum initial values. Later, during the transition period, they drop rapidly and once the flow is fully turbulent a period of slow decay sets in. This behaviour is retrieved in almost all the cases except for the SM model. The latter severely under-predicts the drop of the mean values. This illustrates the well-known property of the SM model, which introduces so much viscosity during the transitional regime that hinders transition to turbulence. Such an excess of dissipation has also been observed by Vreman *et al.* [39], in his study of a turbulent mixing layer. On the opposite, the use of BM model results in an earlier decrease of the mean values along the centreline. Remember that the BM model has a serious flaw; it is not dissipative. This means that the calculation becomes

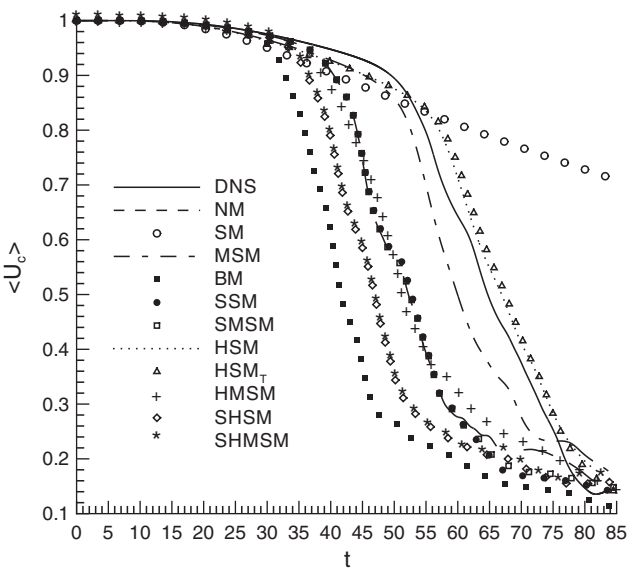

Figure 4. Temporal evolution of the mean centreline axial velocity.

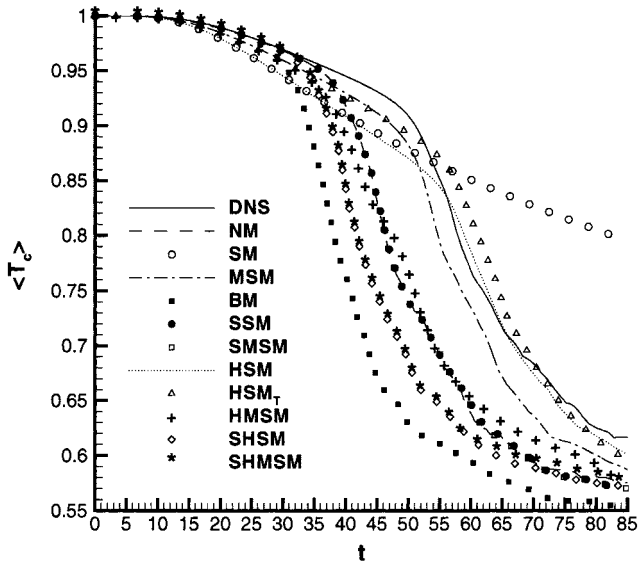

Figure 5. Temporal evolution of the mean centreline temperature.

unstable because flow scales are under-resolved on the coarser grid and there is no subgrid viscosity to damp these instabilities. Moreover all the models involving the selective function give even worst or quasi-equal predictions than NM. The models MSM and HSM do improve the results. This illustrates two properties: both the linear combination of the SM model with the similarity model and the use of a dynamic adjustment of the SM coefficient meet the major shortcoming of the Smagorinsky model, namely the excessive dissipation in the transitional regime.

In the HSM calculation the hybrid model only applies to the subgrid stress tensor. We also perform a LES simulation with a hybrid model for both the subgrid tensor and the subgrid heat flux B_l (see Equation (49) in Section 3). The latter calculation is referred to HSM_T in figures. First, results show that the use of a hybrid model for B_l does not affect the evolution of the mean centreline velocity (see Figure 4). Second, HSM_T and HSM calculations do not exhibit significant differences, except maybe at the beginning of the transition processes, where HSM_T compares much better with DNS results than HSM.

Profiles of mean streamwise velocity and mean temperature normalized by their respective centreline values are plotted in Figures 6 and 7 for the different models and the well-resolved DNS. These profiles are obtained using the method described in the previous paragraph and results are presented at different times of the simulation. Qualitative features deduced from the analysis of the previous figures are confirmed. We first look at the velocity profiles. At the beginning of the transition process, all the models fit the curve relative to the well-resolved DNS calculation (data not shown). Then, as the simulation progresses in time, the round jet spreads for the contribution of perturbations. This spreading is over estimated for the models which results show an earlier decay of the centreline velocity (see for example the curves relative to the BM calculation in Figures 4 and 6), while it is under estimated for the SM model.

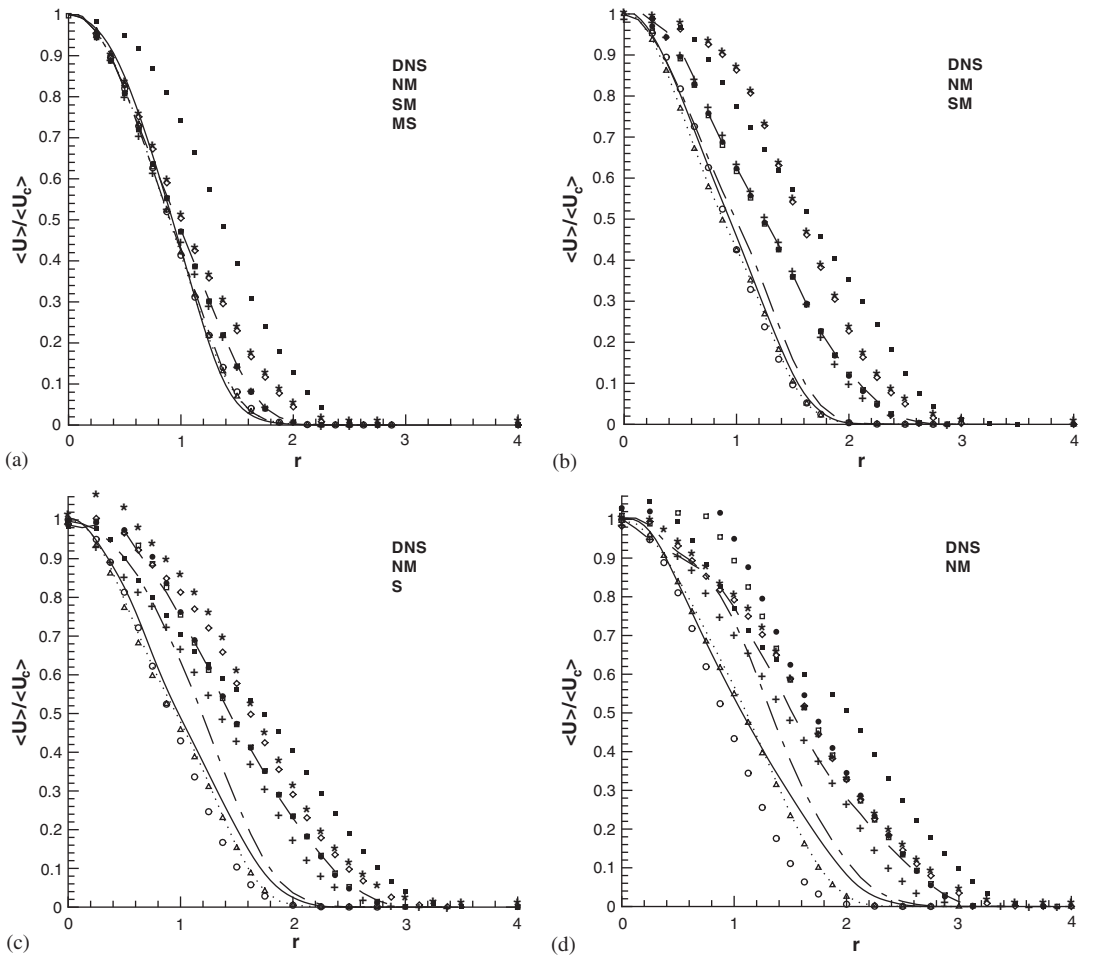

Figure 6. Profiles of mean axial velocity normalized by the mean centreline velocity: (a) $t = 45$, (b) $t = 55$, (c) $t = 60$, (d) $t = 65$.

Similar conclusions are obtained for the evolution of the temperature distribution. We can also notice that the agreement between the HSM or (HSM_T) model and the well resolved DNS simulation is better achieved in the external region of the jet ($r \geqslant 1.2$) than in the core, as observed in Figure 7(d). Furthermore, when comparing Figures 6(d)–7(d), we can remark that the thermal field spreads faster than the velocity one. At this stage, the temperature variations are supposed to be sufficiently weak so that any physical reasoning would lead one to conclude that the temperature is a passive scalar. Consequently the profiles would be coincident. This apparent anomaly was experimentally observed by Davies *et al.* [41]. They investigated the case of an heated jet, where the temperature difference with respect to the ambient was small enough to be considered as a passive scalar.

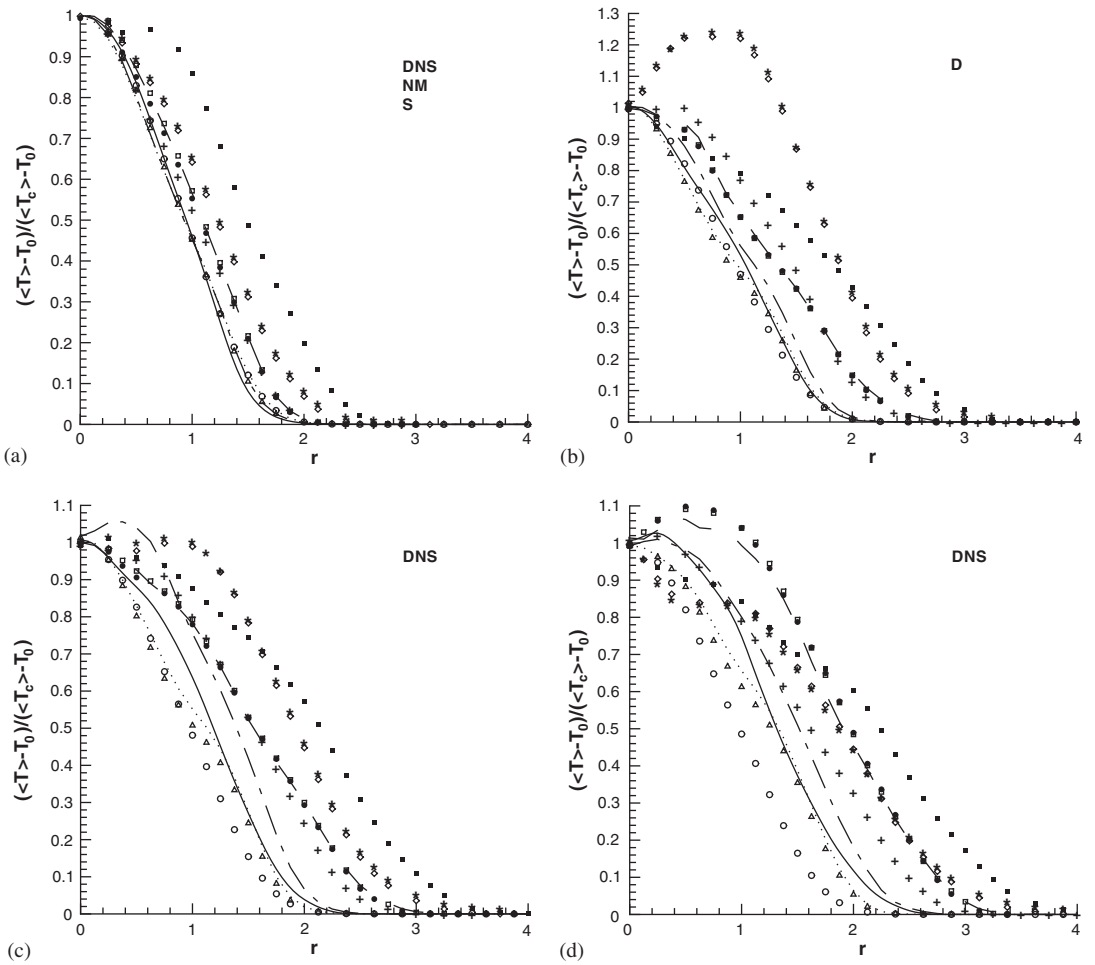

Figure 7. Profiles of mean temperature normalized by the mean centreline temperature: (a) $t = 45$, (b) $t = 55$, (c) $t = 60$, (d) $t = 65$.

Finally, HSM (or HSM_T) and MSM models improve the results. Moreover, HSM (or HSM_T) most closely approaches the DNS mean temperature and velocity profiles.

6.2.2. Evolution of turbulent kinetic energy. Figure 8(a) shows the temporal evolution of the turbulent kinetic energy. It is calculated as follows. First a spectrum is acquired by taking the Fourier transform of the velocity field in the periodic direction, and integrating the Fourier coefficients in the x, z plane. Finally turbulent kinetic energy is obtained by adding the values of the one-dimensional spectrum up all wavenumbers. The subgrid scale and molecular dissipation integrated over the domain are shown in Figures 8(b) and 8(c) respectively. The integration is performed with the trapezoidal rule. Subgrid dissipation ε_{sgs} illustrates the effect of the subgrid models, that is the amount of energy drained by the subgrid scales. On the other hand, molecular dissipation ε_{mol} is relative to the presence of small scales. Both

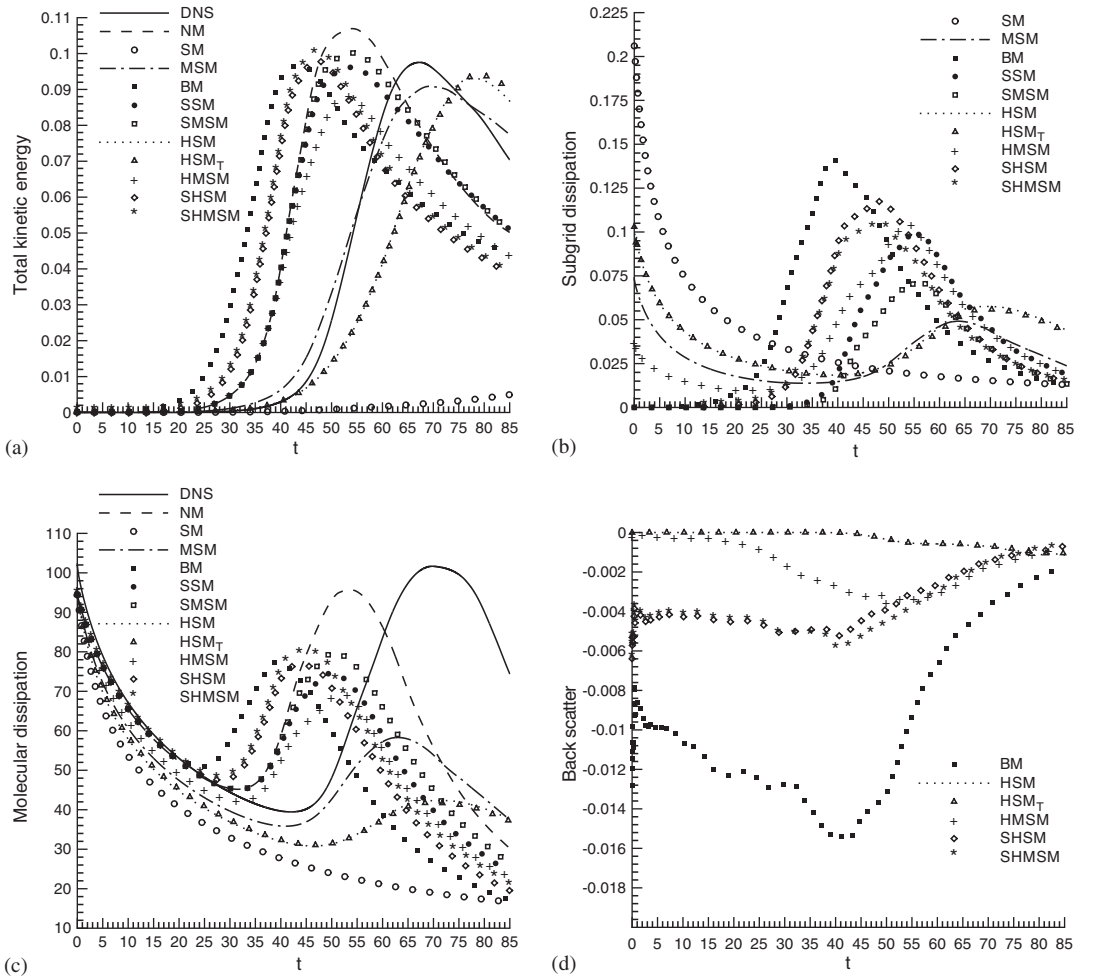

Figure 8. Temporal evolution of the: (a) total kinetic energy, (b) subgrid dissipation, (c) molecular dissipation and (d) backscatter.

molecular and subgrid scale dissipations are involved in the evolution of the total energy and defined as

$$\varepsilon_{\mathrm{mol}} = \mu \tilde{S}_{ij} \partial_j \tilde{u}_j \tag{58}$$

$$\varepsilon_{\mathrm{sgs}} = -\bar{\rho} \tau_{ij} \partial_j \tilde{u}_j \tag{59}$$

The molecular dissipation is always positive whereas the subgrid one can be positive or negative. If it is positive, the subgrid scales remove energy from the resolved ones (forward scatter); if it is negative they release energy to the resolved scales (backscatter). For eddy viscosity-type models, $\varepsilon_{\mathrm{sgs}}$ is always positive. These models are absolutely dissipative and

therefore can only account for forward scatter. Only the cases of hybrid or similarity models can provide negative subgrid dissipation. The amount of backscatter is presented in Figure 8(d) for the models of concern and is calculated as follows:

$$\int_{\Omega} \min(\varepsilon_{\mathrm{sgs}}, 0)\, \mathrm{d}x \tag{60}$$

In Figure 8(a), the conclusions relative to the previous figures are confirmed. The excessive dissipation of the SM is so important that it erases the instabilities and therefore inhibits the increase of the turbulent kinetic energy. Figure 8(b) clearly reveals this excess of subgrid scale dissipation early in the simulation, while in Figure 8(c), the absence of small scales of turbulence is ensured by the fall of the molecular dissipation during all the calculation. On the opposite, the transition is too rapid for the BM calculation. Selective models as well as HMSM and NM lead to similar observations. In these former cases the amount of turbulent energy is expected to be due to the presence of too many small scales. At the beginning, the subgrid scale dissipation provided by the former models is not enough significant to be able to damp the initial perturbations (see Figure 8(b)). For example, if we consider the curves relative to the SSM simulation, subgrid scale dissipation begins to act at $t \approx 40$, which is too late. Thus, as shown in Figure 8(c) by an earlier increase in the molecular dissipation, SSM allows the development of non-physical fluctuations (or the presence of small scales) resulting from the insufficient resolution of the coarser grid. Moreover, for BM and all hybrid models, the mechanism of backscatter indicates a reversal of the energy cascade wherein large scales absorb energy from the small ones and consequently participates to the evolution of energy. However, as shown in Figure 8(d), in the worst of the investigated cases (maximum of backscatter), namely the BM model, the amount of backscatter only represents about 10% of the forward scatter, and the insufficient viscosity is still believe to be responsible for the earlier growth of the turbulent energy. Furthermore, we can notice that the use of the selective function accentuates the backscatter phenomenon. This is particularly evident when comparing the curves relative to HSM (or $\mathrm{HSM_T}$) and SHSM simulations in Figure 8(d). For the HSM (or $\mathrm{HSM_T}$) the increase of energy is slightly delayed while it is better predicted by the MSM model. Indeed, until $t \approx 50$ in Figure 8(b), the subgrid dissipation provided by the HSM (or $\mathrm{HSM_T}$) is greater than that of the MSM. So HSM (or $\mathrm{HSM_T}$) introduces too much subgrid viscosity which eliminates more small scales than the MSM does. This is confirmed by the evolution of the molecular dissipation in Figure 8(c), which remains smaller for HSM (or $\mathrm{HSM_T}$) than for MSM. It also helps to explain the differences observed in Figure 4: the decrease of the centreline velocity appears earlier with the MSM model than with the HSM (or $\mathrm{HSM_T}$) model.

6.2.3. Turbulent stresses and turbulent heat flux. Another important feature allowing to characterize the accuracy of a subgrid model is its correlation with the real velocity and temperature fluctuations provided by the well resolved DNS data. Therefore, the ability of the different models to reproduce the details of these turbulent intensities is addressed in the present paragraph. In the case of round jet flow simulations, profiles of turbulent stresses are often formulated in cylindrical co-ordinates [30, 42], and we will therefore adopt this configuration. Figures 9 and 10 present comparisons of the spatially averaged turbulence components at $t = 65$, well beyond the beginning of the transition processes. At this time, the mean centreline velocity has already lost about 50% of its initial maximum value (see Figure 4, DNS

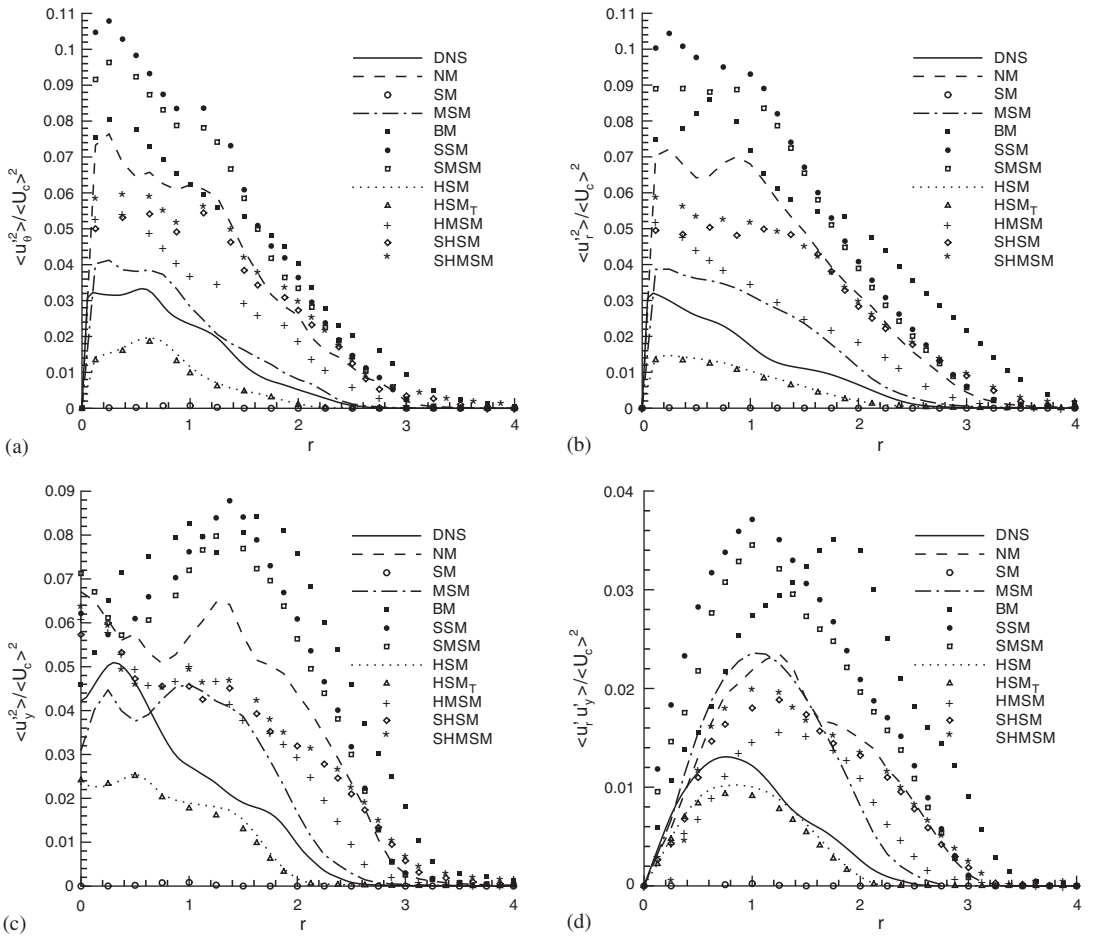

Figure 9. Profiles of mean normalized turbulent intensities at $t = 65$: (a) $\langle u_\theta'^2 \rangle / \langle U_c \rangle^2$, (b) $\langle u_r'^2 \rangle / \langle U_c \rangle^2$, and (c) $\langle u_y'^2 \rangle / \langle U_c \rangle^2$, (d) $\langle u_r' u_y' \rangle / \langle U_c \rangle^2$.

calculation). These latter are computed in this paper as follows. First, the instantaneous field ϕ_i (temperature or velocity) is interpolated into a polar grid. Second, we compute the Fourier transform of each velocity and temperature component. We next obtain the turbulent intensities, which are defined as

$$|\phi_i' \phi_j'| = \hat{\phi}_i(x, z, k_y, t) \hat{\phi}_j^t(x, z, k_y, t) \tag{61}$$

Here $\hat{\phi}_i$, $\hat{\phi}_j^t$ and k_y denote the Fourier transform of the velocity or temperature component, the complex conjugate of the Fourier transform velocity or temperature component and the wave number in the axial direction, respectively. Finally $\langle \phi_i' \phi_j' \rangle$ is computed by taking simple average over all points in the homogeneous direction.

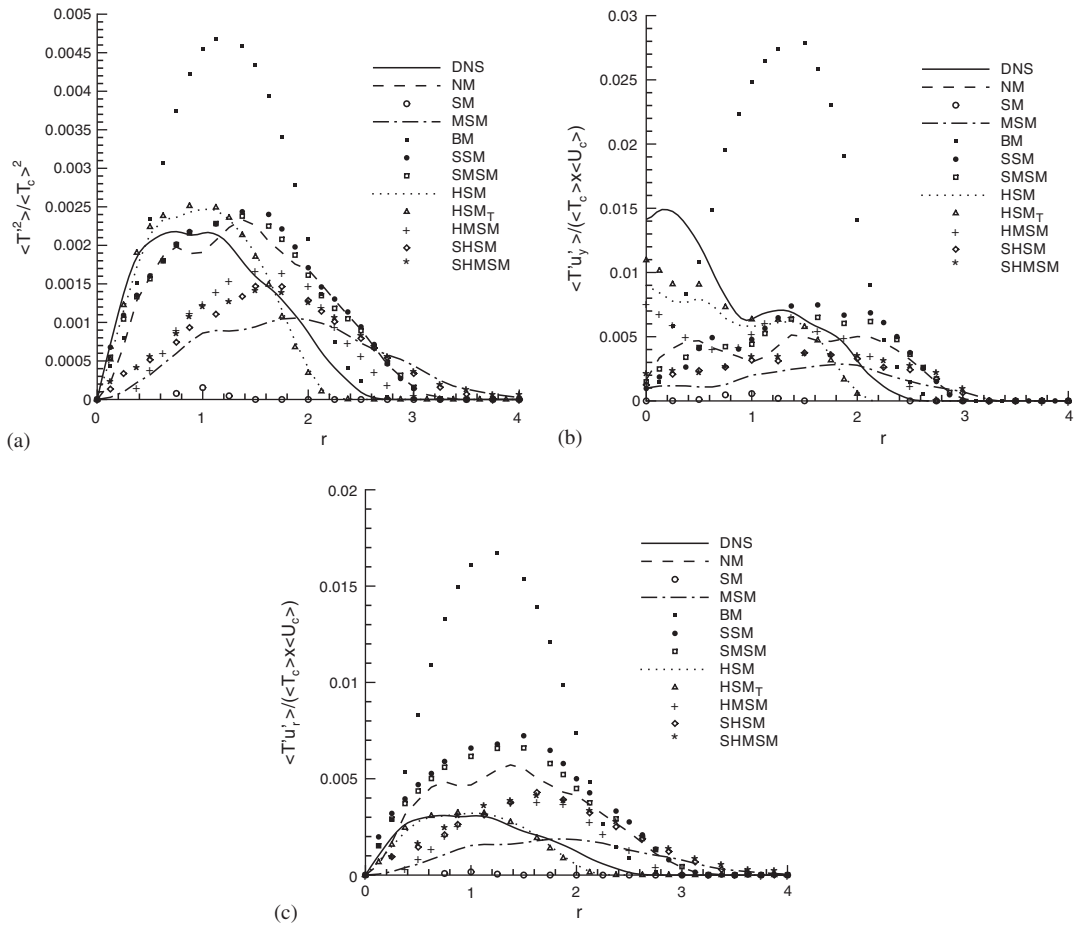

Figure 10. Profiles of mean normalized turbulent intensities at $t = 65$: (a) $\langle T'^2 \rangle / \langle T_c \rangle^2$, (b) $\langle T' u'_y \rangle / (\langle T_c \rangle \langle U_c \rangle)$, (c) $\langle T' u'_r \rangle / (\langle T_c \rangle \langle U_c \rangle)$.

All selective models as well as BM, NM, SM and HMSM do not agree satisfactory. HSM and $\mathrm{HSM_T}$ calculations give similar results. From a qualitative point of view, the agreement between DNS and LES results is reasonably good for HSM (or $\mathrm{HSM_T}$) and MSM models, as shown in Figure 9. However, the magnitudes of the stresses are not retrieved. Indeed, LES only involves the large-scale contribution while DNS also includes the small scale one, therefore a quantitative agreement between DNS and LES results cannot be expected. However, Figure 10 clearly demonstrates that the MSM model is unable to reproduce the structure of the fluctuating temperature and turbulent heat flux fields, while they are qualitatively predicted by the HSM (or $\mathrm{HSM_T}$) model.

6.2.4. Flow visualizations. The aim of the present paragraph is to test the ability of the subgrid models to capture the jet flow topology during its transition to a fully turbulent state.

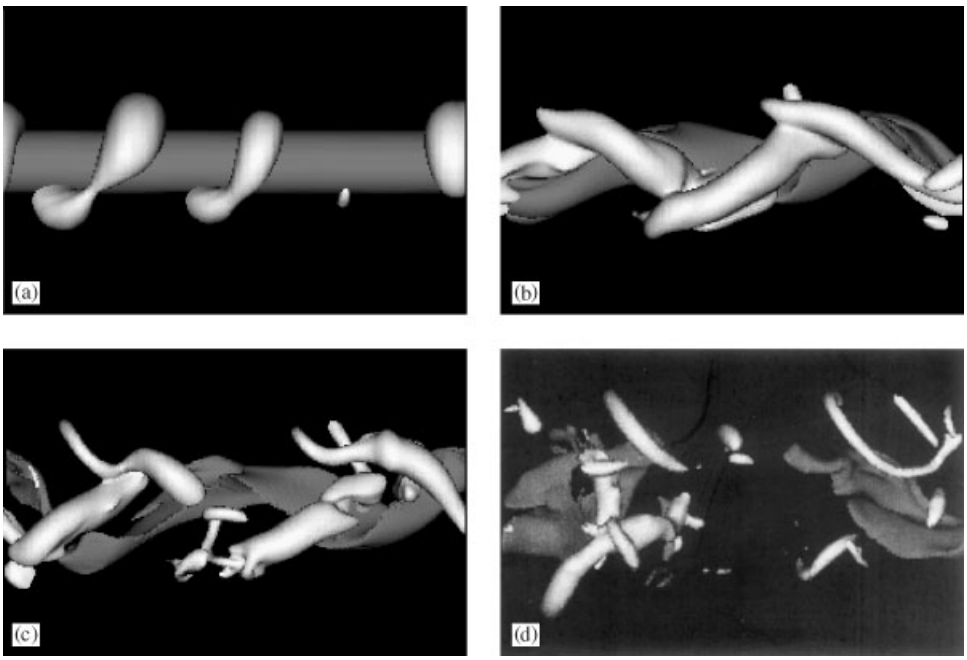

Figure 11. Well resolved DNS calculation. Tridimensional view of the pressure (bright surfaces) and the density (dark surfaces) fields. Pressure surfaces satisfy the relation $P_{iso} = P_i + 0.2 \times (P_{min} - P_i)$, where P_i and P_{min} denote the initial uniform pressure value and the minimum pressure value at the time considered, respectively. Density surfaces correspond to the minimum density value at the time considered. (a) $t = 20$, (b) $t = 60$, (c) $t = 65$, (d) $t = 75$.

Figure 11 is relative to the DNS simulation. We present the temporal evolution of constant pressure surfaces P_{cst} and constant density surfaces ρ_{cst}, which satisfy the following relations:

$$P_{cst} = P_i + (P_{min} - P_i) \times 0.2 \tag{62}$$

$$\rho_{cst} = \rho_{min} \tag{63}$$

where P_i, P_{min} and ρ_{min} are the initial uniform pressure value, the minimum pressure value and the minimum density value at the time considered, respectively. Pressure surfaces are used to visualized the development of perturbations whereas constant density surfaces rather provide a good definition of the jet and external flow interface. This kind of visualization was first introduced by Fouillet [43] in his study of compressibility effects upon a round jet. In Figure 11(a) ($t = 20$), large structures of pressure surface appear as rings around density surface and make up a helix. In Figure 11(b) the structures of pressure surface undergo a connection and characterizes the end of the transitional regime. Later, while turbulent kinetic energy decreases, the pressure as well as the density fields fragment, and the jet flow breaks down into turbulence (see Figures 11(c) and 11(d)). So, the growth of the fundamental instability is strongly related to the temporal evolution of the turbulent kinetic energy, and it is expected that the conclusions deducted from this later quantity remain valid when the topology of the

Figure 12. NM calculation at $t = 60$. Tridimensional view of the pressure (bright surfaces) and the density (dark surfaces) fields. Pressure surface satisfies the relation $P_{iso} = P_i + 0.2 \times (P_{min} - P_i)$, where P_i and P_{min} denote the initial uniform pressure value and the minimum pressure value at the time considered, respectively. Density surface corresponds to the minimum density value at the time considered.

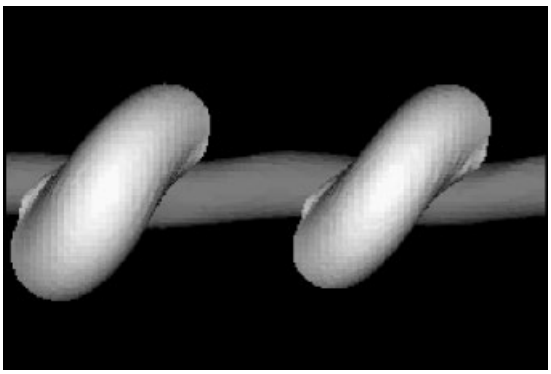

Figure 13. SM calculation at $t = 75$. Tridimensional view of the pressure (bright surfaces) and the density (dark surfaces) fields. Pressure surface satisfies the relation $P_{iso} = P_i + 0.2 \times (P_{min} - P_i)$, where P_i and P_{min} denote the initial uniform pressure value and the minimum pressure value at the time considered, respectively. Density surface corresponds to the minimum density value at the time considered.

flow is of interest. Therefore, we will first examine the case in which an earlier increase of the energy is observed and which may therefore exhibit an earlier transition into fully turbulent state. As an example we examine the case of the NM simulation in Figure 12 ($t = 60$). Obviously, the insufficient resolution of the coarser grid accelerates the evolution of the jet, such that at $t = 60$ the flow already exhibits a turbulent comportment while, at the same time, the DNS results only show the connection of the pressure rings. This also confirms the presence of too many small scales early in the simulation. Similar conclusions hold for BM, SHSM, SHMSM, NM, SMSM, SSM and HMSM models as well (data not shown). If we now look at the SM results, which severely delay the growth of the turbulent kinetic energy and consequently hinders transition to turbulence, we will not be surprised to see in Figure 13 that the pressure rings still dominate the jet behaviour until $t = 75$. HSM and HSM_T simulations provide very similar results. Figures 14 and 15 display the temporal

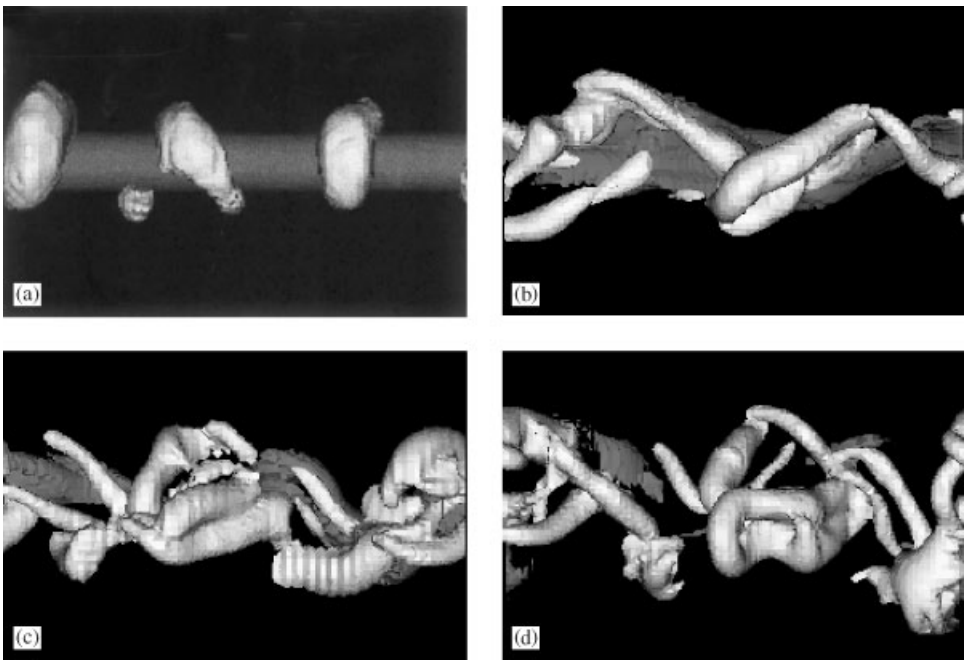

Figure 14. MSM calculation. Tridimensional view of the pressure (bright surfaces) and the density (dark surfaces) fields. Pressure surfaces satisfy the relation $P_{iso} = P_i + 0.2 \times (P_{min} - P_i)$, where P_i and P_{min} denote the initial uniform pressure value and the minimum pressure value at the time considered, respectively. Density surfaces correspond to the minimum density value at the time considered. (a) $t = 20$, (b) $t = 60$, (c) $t = 65$, (d) $t = 75$.

evolution of pressure and density constant surfaces for the MSM model and the HSM model, respectively. Among the models considered in our study and concerning the jet flow topology, the MSM and HSM (or HSM_T) models provide undoubtedly the best results. The scenario for the DNS is correctly reproduced, however HSM (or HSM_T) results are smoother than MSM ones. This is particularly evident when comparing Figure 14(c) and 15(c). For this latter reason we consider that HSM (or HSM_T) model provides better results than the MSM model.

7. SUMMARY AND CONCLUSIONS

In this paper, we have presented *a posteriori* tests in the case of a temporally developing heated round jet at a low Mach number. Nine subgrid models have been investigated for the subgrid stress tensor and the subgrid heat flux in the filtered energy equation as well. The adequacy of nine subgrid models has been achieved by comparisons with our direct numerical simulation. Therefore, to allow correspondence between DNS and LES, the Reynolds number in the present study is still not very high. In order to provide a point of reference for the subgrid models, we have also performed a DNS on the coarse LES grid. This calculation corresponds to the case in which the subgrid terms are simply omitted.

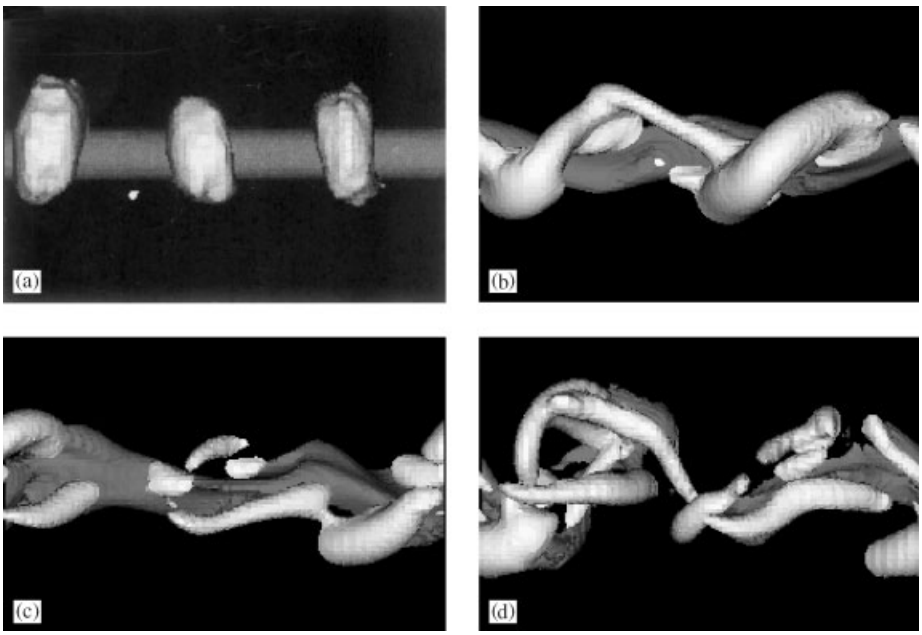

Figure 15. HSM calculation. Tridimensional view of the pressure (bright surfaces) and the density (dark surfaces) fields. Pressure surfaces satisfy the relation $P_{iso} = P_i + 0.2 \times (P_{min} - P_i)$, where P_i and P_{min} denote the initial uniform pressure value and the minimum pressure value at the time considered, respectively. Density surfaces correspond to the minimum density value at the time considered. (a) $t = 20$, (b) $t = 60$, (c) $t = 65$, (d) $t = 75$.

In the present work, the turbulent jet of interest is non-isothermal and the initial temperature difference with respect to the ambient is chosen according to the one at the nozzle exit of a typical aircraft engine. So the aim of the present work was to demonstrate the ability of LES to reproduce both the details of the dynamic and thermal fields accurately.

Some characteristic behaviours of the subgrid scale models were confirmed such as the excessive dissipation of the Smagorinsky model which hinders transition to turbulence, or the production of too many small scales introduced by the similarity modelling. We have also demonstrated that the use of the selective function does not provide any improvement. Finally, the mixed-scale model and the hybrid Smagorinsky model give satisfactory results. However, the hybrid Smagorinsky model is preferred over adopting the mixed-scale model essentially because it provides a much better representation of the stresses and the turbulent heat flux.

REFERENCES

1. Lubbers CL, Brethouwer G, Boersma BJ. Simulation of the mixing of a passive scalar in a round turbulent jet. *Fluid Dynamics and Research* 2001; **28**:189–282.
2. Constantinescu GS, Lele S. Large eddy simulation of a near sonic turbulent jet and its radiated noise. *AIAA paper* 2000-0376, 2001.
3. Ferreira Gago C, Brunet S, Garnier F. Numerical investigation of turbulent mixing in a jet/wake vortex interaction. *AIAA Journal* 2002; **40**:276–284.
4. Zhao W, Franfel SH. Numerical simulations of sound radiated from an axisymmetric premixed reacting jet. *Physics of Fluids* 2001; **13**:2671–2681.

5. Le Ribault C, Sarkar S, Stanley SA. Large eddy simulation of a plane jet. *Physics of Fluids* 1999; **10**: 3069–3083.
6. Tanna HK, Dean PD, Fisher MJ. The influence of temperature on shock-free supersonic jet noise. *Journal of Sound and Vibration* 1975; **39**(4):429–460.
7. Jacquin L, Garnier F. On the dynamics of engine jets behind a transport aircraft. In the characterization and modification of wake from lifting vehicles in fluids. *AGARD* CP-584, 1996; 37.1–37.8.
8. Cortesi AB, Smith BL, Yadigaroglu G, Banerjee S. Numerical investigation of the entrainment and mixing processes in neutral and stably-stratified mixing layers. *Physics of Fluids* 1999; **11**(1):162–185.
9. Schlichting H. Boundary-layer theory. *McGraw-Hill Series in Mechanical Engineering*. McGraw-Hill: New York, 1968.
10. Vreman B. Direct and large eddy simulation of the compressible turbulent mixing layer. *Ph.D. Thesis*, University of Twente, 1995.
11. Favre A. Equations statistiques aux fluctuations turbulentes dans les écoulements compressibles: cas des vitesses et des températures. *Comptes Rendus des Seancesde l'Academie des Sciences de Paris* 1971; **273**(A): 1087–1093.
12. Smagorinsky J. General circulation experiments with the primitive equations. *Monthly Weather Review* 1963; **91**(3):99–165.
13. Clark RA, Ferziger JH, Reynolds WC. Evaluation of subgrid-scale models using an accurately simulated turbulent flow. *Journal of Fluid Mechanics* 1979; **91**(1):1–16.
14. Deardorff JW. On the magnitude of the subgrid scale eddy viscosity coefficient. *Journal of Computational Physics* 1971; **7**:120–133.
15. Erlerbacher G, Hussaini MY, Speziale CG, Zang TA. Toward the large-eddy simulation of compressible turbulent flows. *Journal of Fluid Mechanics* 1992; **238**:155–185.
16. Piomelli U, Zang, TA, Speziale CG, Hussaini MY. On the large-eddy simulation of transitional wall-bounded flows. *Physics of Fluids* 1990; **A2**(2):257–264.
17. Sagaut P, Troff B, LE TH, Dang-Tran K, Ta Phuoc L. Large-eddy simulation of turbulent flow past a backward facing step with a new mixed-scale SGS model. *IMACS-COST Conference-Computational Fluid Dynamics-Three-Dimensional Complex Flows*, Lausanne (Switzerland), September 13–15, 1995.
18. Sagaut P, Crohens R. Discrete filters for large-eddy simulation. *International Journal for Numerical Methods in Fluids* 1999; **31**:1195–1220.
19. Sagaut P. Introduction à la simulation des grandes échelles pour les écoulements de fluide incompressible. *Collection Mathématiques et Applications*, vol. 30. Springer: Berlin, 1998.
20. Bardina J, Ferziger JH, Reynolds WC. Improved turbulence models based on large eddy simulation of homogeneous, incompressible, turbulent Flows. *Report* TF-19, Thermosciences Division, Department of Mechanical Engineering, Stanford University, 1983.
21. Liu S, Meneveau C, Katz J. On the properties of similarity subgrid-scale models as deduced from measurements in a turbulent Jet. *Journal of Fluid Mechanics* 1994; **275**:83–119.
22. Lenormand E, Sagaut P, Ta Phuoc, L. Large eddy simulation of subsonic and supersonic channel flow at moderate Reynolds number. *International Journal for Numerical Methods in Fluids* 2000; **32**:369–406.
23. Horuiti K. The role of Bardina model in large-eddy simulation of turbulent channel flow. *Physics of Fluids* 1989; **A1**(2):426–428.
24. David E. Modélisation des écoulements compressibles et hypersoniques: une approche instationnaire. *Ph.D. Thesis*, Institut National Polythechnique de Grenoble, Juin 1993.
25. Sagaut P, Troff B. Subgrid scale improvements for non-homogeneous flows. *First AFOSR International Conference on DNS and LES*, Ruston, USA, 1997.
26. Sarkar S, Erlerbacher G, Hussaini MY, Kreiss HO. The analysis and modelling of dilatational terms in compressible turbulence. *Journal of Fluid Mechanics* 1991; **227**:473–493.
27. Zang TA, Dahlburg RR, Dahlburg JP. Direct and large eddy simulation of three dimensional compressible Navier–Stokes turbulence. *Physics of Fluids* 1992; **A4**(1):127–140.
28. Ghosal S, Lund TS, Moin P, Akselvoll K. A dynamic localization model for large eddy simulation of turbulent flows. *Journal of Fluid Mechanics* 1995; **286**:229–255.
29. Lele SK. Compact finite difference scheme with spectral-like resolution. *Journal of Computational Physics* 1992; **103**:16–42.
30. Boersma BJ, Lele SK. Large eddy simulation of a Mach 0.9 turbulent jet. *AIAA Paper* 99-1874, 1999.
31. Lowery PS, Reynolds WC. Numerical simulation of a spacially developing forced plane mixing layer. *Report* NoTF-26, Stanford University, 1986.
32. Michalke A, Hermann G. On the inviscid instability of a circular jet with external flow. *Journal of Fluid Mechanics* 1982; **114**:343–359.
33. Gaster M. A note on the relation between temporally-increasing and spatially-increasing disturbances in hydrodynamic stability. *Journal of Fluid Mechanics* 1962; **14**:222–224.
34. Thompson KW. Time dependent boundary conditions for hyperbolic system II. *Journal of Computational Physics* 1990; **89**:439–461.

35. Crighton DG, Gaster M. Stability of slowly diverging jet flow. *Journal of Fluid Mechanics* 1976; **77**:397–413.
36. Morris PJ. The spatial viscous instability of axisymmetric jets. *Journal of Fluid Mechanics* 1976; **77**:511–529.
37. Plaschko P. Helical instabilities of slowly divergent jets. *Journal of Fluid Mechanics* 1979; **92**:209–215.
38. Moore CJ. The role of shear-layer instability waves in jet exhaust noise. *Journal of Fluid Mechanics* 1977; **80**:321–367.
39. Vreman B, Geurts B, Kuerten H. Large-eddy simulation of the turbulent mixing layer. *Journal of Fluid Mechanics* 1997; **339**:357–390.
40. Verzicco R, Orlandi P. Direct simulations of the transitional regime of a circular jet. *Physics of Fluids* 1994; **6**(2):751–759.
41. Davies AE, Keffer JF, Baines WD. Spread of a heated plane turbulent jet. *Physics of Fluids* 1975; **18**(7): 770–775.
42. Freund JB. Noise sources in a low-Reynolds-Number turbulent jet at Mach 0.9. *Journal of Fluid Mechanics* 2001; **438**:227–305.
43. Fouillet Y. Contribution à l'étude par expérimentation numérique des écoulements libres cisaillés: effets de compressibilité. *Ph.D. Thesis*, Institut polytechnique de Grenoble, 1991.

